

Simulation of the Sedimentation of a Falling Oblate

F. Fonseca and H. J. Herrmann

ICA1, University of Stuttgart, Pfaffenwaldring 27, 70569 Stuttgart, Germany.

(November 2, 2018)

We present a numerical investigation of the dynamics of one falling oblate ellipsoid particle in a viscous fluid, in three dimensions, using a constrained-force technique [19], [20] and [17]. We study the dynamical behavior of the oblate for a typical downward motion and obtain the trajectory, velocity, and orientation of the particle. We analyze the dynamics of the oblate generated when the height of the container, the aspect-ratio, and the dynamical viscosity are changed. Three types of falling motions are established: steady-falling, periodic oscillations and chaotic oscillations. In the periodic regime we find a behavior similar to the case of falling flat strips reported in ref. [13]. In the chaotic regime the trajectory of the oblate is characterized by a high sensitivity to tiny variations in the initial orientation. The Lyapunov exponent is $\lambda = 0.052 \pm 0.005$. A phase space comparing to the results of ref [12], is shown.

I. INTRODUCTION

The way in which objects fall to the ground has been studied since antiquity. Objects were thought to return to “their natural” places by the ancient Greeks. Newton showed that the bodies fall on earth driven by a constant acceleration. But despite gravity’s undeniable attraction, not all falling objects travel downwards on straight trajectories. The tree leaves flutter to the ground in the autumn, exhibiting a complex motion and refusing to follow the shortest path.

A deep understanding of the motion of falling objects in a fluid is of great technical importance, and has been investigated in a variety of contexts, including meteorology [1], aircraft stability [2], power generation [3], chemical engineering [4], etc. Also Newton observed the complex motion of objects falling in both air and water [6]. This phenomenon was also studied by Maxwell, who discussed the motion of a falling paper strip [7].

In the nineties, Aref and Jones [10] found through numerical solutions of Kirchhoff’s equations that the trajectory for an object moving through an incompressible inviscid and irrotational fluid, is chaotic. Tanabe and Kaneko [9], using a phenomenological model for the falling of a one-dimensional (1D) piece of paper, including lift and dynamical viscosity, but neglecting the inertia of the fluid, describe five falling regimes. Two of them are chaotic. In 1997 Stuart B. Field et al. [12], investigated experimentally the behavior of falling disks in a fluid, and identified different dynamical regimes as function of the moment of inertia and the Reynold’s number. They obtained experimental evidence for chaotic intermittency [11]. In 1998 Andrew Belmonte, et al. [13], in an experiment with thin flat strips falling through a fluid, observed only two motions: side to side oscillation (flutter) and end-over-end rotation (tumbling). They proposed a phenomenological model including inertial drag and lift which reproduces this motion, and yields the Froude similarity, which describes the transition from flutter to tum-

ble regime. Mahadevan et al [23], in 1999 made an experiment of dropping horizontal cards of thickness d and width w , showing that the tumbling frequency Ω scales as $\Omega \approx d^{1/2}w^{-1}$, consistent with a dimensional argument that balances the drag against gravity.

Given the difficulties to study this problem theoretically and experimentally, we took a computational approach simulating the falling of one oblate ellipsoid in a viscous fluid in a three dimensional container. An oblate is an ellipsoid for which the two largest principal radii are equal. We organize the paper in the following manner. In section 2 we give an review over the model that we use. In Sec. 3A we describe the main features of the falling oblate. In Sec. 3B-D we present the results for the change in the initial height, the oblate’s aspect-ratio and the dynamical viscosity, for the steady-falling regime. In sec. 3E we show the periodic behavior and compare to the results of reference [13]. In Sec. 3F the sensitivity to tiny variations in the oblate’s initial orientation is presented in the chaotic regime. In sec. 3G the parameter phase space is sketched and compared to the results of reference [12]. Section 4 summarizes present results and discusses possible further applications.

II. MODEL

The general idea, proposed by Fogelson and Peskin [21], is to work with a simple grid for the resolution of the fluid motion at all times and represent the particles not as boundary conditions to the fluid, but by a volume force term or Lagrange multipliers in the Navier Stokes equations.

This technique was developed in the work of Kuusela, et al [17], Wachmann, et al [18] and Hoeffler et al. [19], [20], and employs a numerical solver for the dynamical simulation of three-dimensional rigid particles in a Newtonian fluid, bounded by a rectangular container.

The motion of the fluid is described by the dimensionless Navier-Stokes equations:

$$\frac{\partial \vec{v}}{\partial t} + (\vec{v} \cdot \nabla) \vec{v} = -\nabla p + \frac{1}{Re} \nabla^2 \vec{v} + \vec{f} \quad (1)$$

Here p and \vec{v} are the pressure and the velocity of the fluid, respectively, and \vec{f} is an external force.

The Reynolds number Re is defined as

$$Re := \frac{UD\rho_f}{\nu} \quad (2)$$

where U is the mean vertical oblate velocity, D a characteristic length that in our case is the largest oblate's diameter, ρ_f the density and ν the dynamical viscosity of the fluid.

For an incompressible fluid, the continuity equation:

$$\frac{\partial \rho_f}{\partial t} + \nabla \cdot (\rho_f \vec{v}) = 0 \quad (3)$$

reduces to

$$\nabla \cdot \vec{v} = 0 \quad (4)$$

Equation (1) is discretized on a regular, marker-and-cell mesh to second order precision in space. For the time stepping, we employ an operator-splitting-technique which is explicit and accurate to first order. The suspending fluid is subjected to no-slip boundary conditions at the surface of the suspended particles. More details of the solution procedure are presented in [17], [19], [20].

The geometry of the oblate ellipsoid is characterized by Δr its aspect-ratio defined as the ratio of the smallest radius over the largest one.

An oblate is represented by a rigid template connected to fluid tracer particles, which are moving on the trajectories of the adjacent fluid. The connection is made by using the body force term, in the Navier-Stokes equations, as constraints on the fluid such to describe the oblate.

The force density \vec{f}^c , is chosen elastic with a spring constant that, and guarantees that the elongation remains small against the grid spacing at all times [18], and it is zero in the exterior of the region outside the oblate. We can define this force density \vec{f}^c as:

$$\vec{f}^c = f^c(x_{ij}^{\vec{r}} + \vec{\epsilon}(x_{ij}^{\vec{r}})) = -k\vec{\epsilon}(x_{ij}^{\vec{r}}) \quad (5)$$

where $x_{ij}^{\vec{r}}$ is the displacement field of the separation between the markers i and their corresponding reference point j . The stiffness constant k , must be chosen large enough so that $|\vec{\epsilon}(x_{ij}^{\vec{r}})| \ll h$, (h size grid), holds for all iterations.

In general the displacement field $\vec{\epsilon}(x_{ij}^{\vec{r}})$ is defined as:

$$\vec{\epsilon}_i(x_{ij}^{\vec{r}}) = x_{ij}^{\vec{m}} - x_{ij}^{\vec{r}} \quad (6)$$

The vector $x_{ij}^{\vec{m}}$ is the position of a fluid tracer, whose motion is determined by the fluid local velocity, i.e.,

$$\dot{x}_{ij}^{\vec{m}} = \vec{u}(x_{ij}^{\vec{m}}) \quad (7)$$

The $x_{ij}^{\vec{r}}$ are the reference points associated to a template having the shape of the physical particle:

$$x_{ij}^{\vec{r}} = \vec{x}_i + O_i(t) \cdot \vec{r}_{ij} \quad (8)$$

Here \vec{x}_i is the center of mass of the template, $O_i(t)$ is the rotation matrix that describes the present orientation of the oblate and \vec{r}_{ij} denote the initial position of the reference points with respect to the center of mass. For the quaternion formulation of the rotation, we use the techniques described in ref. [15].

A velocity-Verlet integrator [16] serves to integrate the equations of motion for the translation and a Gear-predictor integrator [5] for the rotation on the template:

$$\vec{F} = -Mg\hat{j} + \rho_f Vg\hat{j} + \sum_i \vec{f}_i^c \quad (9)$$

where \hat{j} is the unit vector along the vertical.

$$\vec{T} = \sum_i (\vec{x}_i - \vec{x}_{cm}) \times \vec{f}_i^c \quad (10)$$

with respect to the template's center of mass \vec{r}_{cm} .

The equations of motion of the particle template are:

$$\dot{\vec{U}} = \frac{\vec{F}}{M} \quad (11)$$

and

$$\dot{\vec{\Omega}} = \frac{\vec{T}}{I} \quad (12)$$

where M is the mass of the template particle; \vec{U} and $\vec{\Omega}$ are the linear and angular velocities of the template particle, respectively; I is the moment of inertia; and \vec{T} is the torque, [17], [19].

The boundary conditions at the container wall are zero for the normal velocity component of the fluid and no-slip condition for the tangential component, because the walls are assumed impenetrable, [19], [18]. The interaction between the oblate and the walls is defined through a contact force, [17], where the walls are treated as a particle with infinite mass and infinite radius.

III. RESULTS

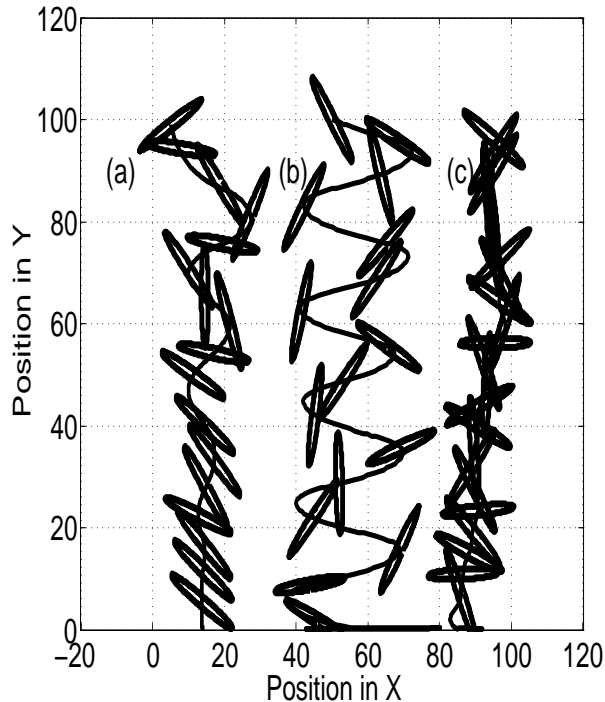


FIG. 1. (a) Steady-falling, (b) Periodic-oscillation, (c) Chaotic motion.

For all our simulations, and in order to reduce the parameter space we use $\rho_{fluid} = 1 \frac{g}{cm^3}$ and $\rho_{oblate} = 3.5 \frac{g}{cm^3}$.

We found three basically different motions in our simulations: steady-falling, side-to-side periodic-oscillation known as 'flutter' ref. [13], and a chaotic motion as shown in fig. 2. The above phenomenology can be compared to the work of ref. [12], for the case of dropping disks. In general, the trajectories depend strongly on the initial conditions and the properties of the system (oblate's orientation Θ_o , dynamical viscosity μ and the oblate's aspect-ratio Δr , etc). We don't find the tumbling motion described in the above references.

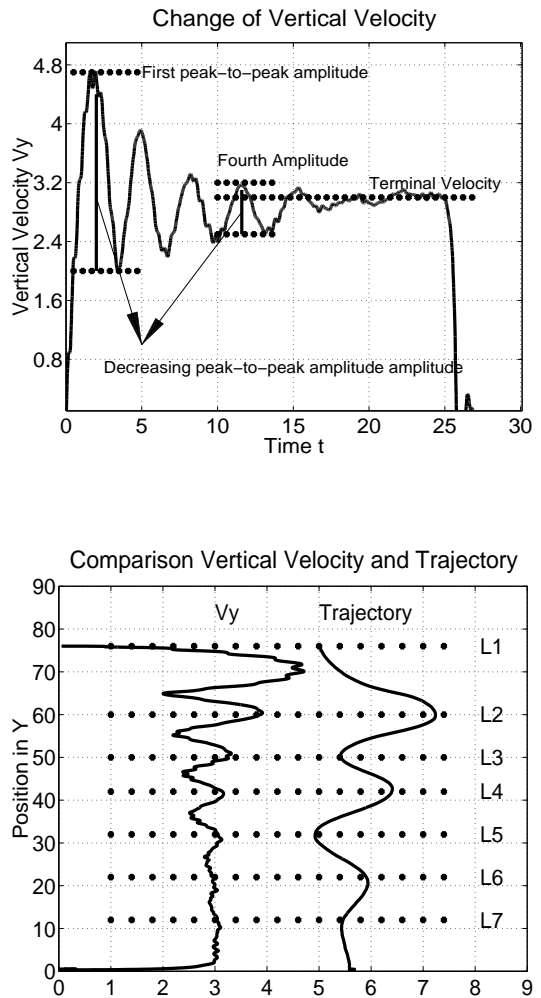


FIG. 2. (top) Decreasing amplitude of the vertical velocity. (bottom) Comparison between the vertical velocity and the spatial trajectory at the same height. Initial conditions of the system. $\theta_o = 26.6^\circ$, $\Delta r = 0.25$, $\mu = 0.033$. Falling initial height $h_o = 76cm$ for the case of steady-falling.

A. Phenomenology of the Steady-Falling Oblate

For the velocity of the center of mass, the vertical component decreases when the oblate approaches the container bottom and shows a damped wavering, with an amplitude that decreases with time (fig. 3 top).

The vertical trajectory is composed of successive turning points, that correspond to the points where the trajectory changes the sign of the rate of change of the vertical velocity component marked in fig. 3(bottom) by the horizontal lines L2, ... L5. We also see, that from L1 to L6 the amplitude for the trajectory and the velocity decrease.

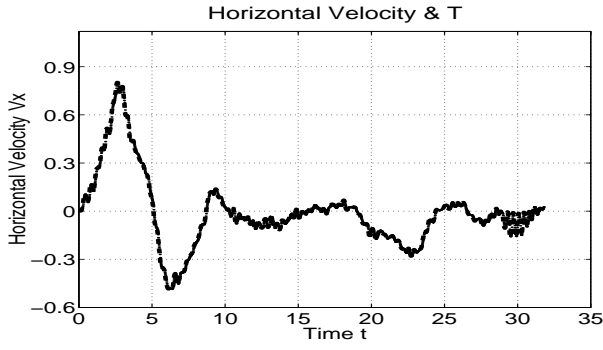


FIG. 3. Horizontal velocity. Initial conditions of the system. $\theta_o = 26.6^\circ$, $\Delta r = 0.25$, $\mu = 0.033$. Falling initial height (b) $h_o = 76\text{cm}$.

The horizontal components of the velocity obey a different behavior as the vertical ones, and in general they have non-regular oscillations as seen in fig.4.

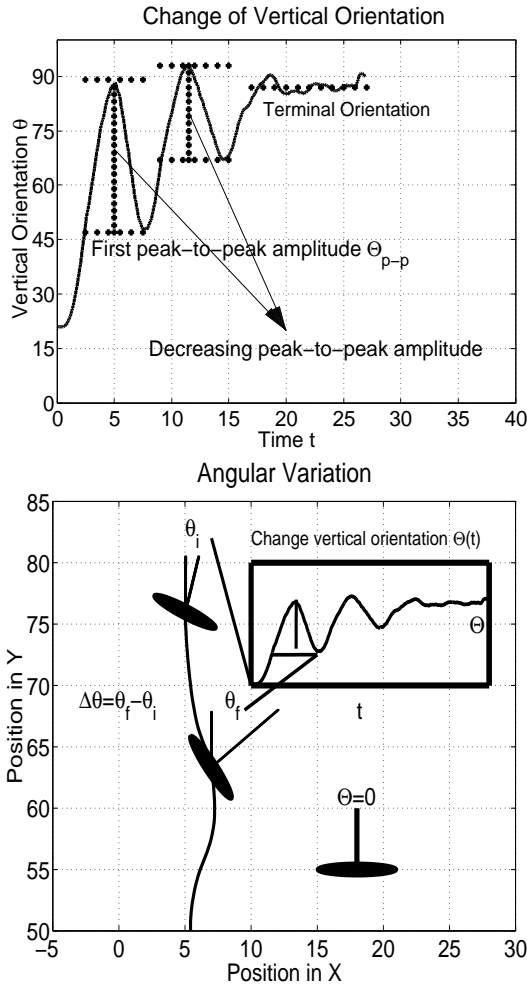


FIG. 4. (Top) Decreasing peak-to-peak amplitude in the angular oscillation. (Bottom) Angular change $\Delta\theta$ along the vertical trajectory. Initial conditions of the system. $\theta_o = 26.6^\circ$, $\Delta r = 0.25$, $\mu = 0.033$. Falling initial height (b) $h_o = 76\text{cm}$.

The oblate orientation is described through the three rotational degrees of freedom, around the center of mass. We present the time evolution of the angle between the oblate's normal and the vertical direction that we will call vertical orientation fig. 5 (top). $\Theta = 0$ implies that the oblate's principal axis will be parallel to the container's horizontal fig. 5 (bottom). At the beginning of the movement, there is a larger angular change of the oblate's normal $\Delta\Theta$ fig. 5(bottom), which is characterized by a larger peak-to-peak amplitude Θ_{p-p} . In fig. 5 the definitions we illustrate the definition of the peak-to-peak amplitude as the distance between successive turning points, which decreases while the oblate sinks. In the steady-falling regime, both the peak-to-peak amplitude Θ_{p-p} and the change $\Delta\Theta = \Theta_f - \Theta_i$, become smaller from the top towards the container's bottom. The oblate tends to align its major axis along the vertical [14], presenting the lowest resistance to its descent in the fluid, and acquiring a limit vertical velocity fig. 3 (top).

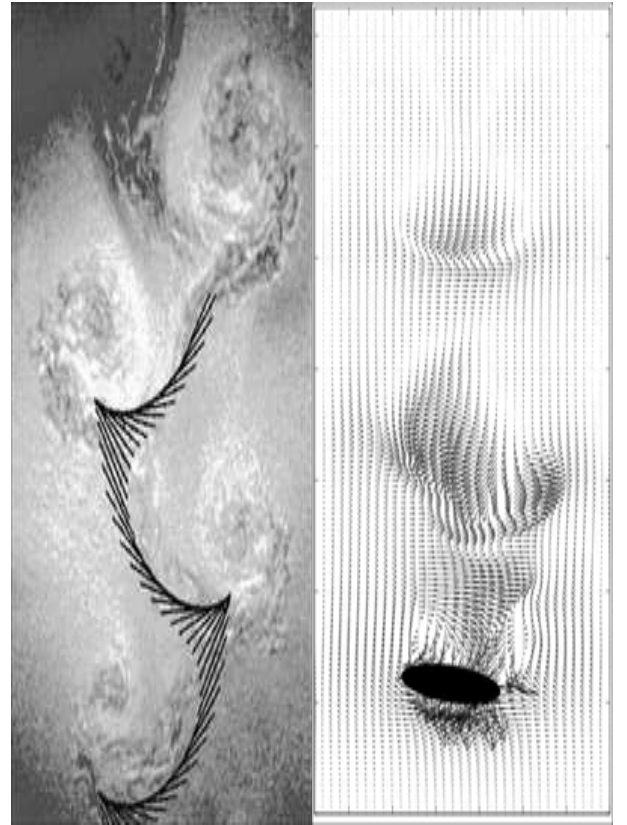


FIG. 5. The right picture shows the vortex structure of the vertical and horizontal components of the fluid velocity field (u, v) generated by the falling oblate, with diameter of 3.2 cm in a container of $10 \times 30 \times 30$ cm and Reynolds number of $Re = 128$, aspect-ratio $\Delta r = 0.5$. The left picture shows shedding vortices reported by Belmonte et al, ref.[12], for a falling strip.

The oblate generates shedding vortices in the fluid along its falling trajectory, an example is shown in figure 6 (right), that shows the velocity fluid field around the oblate, and the vortex is localized just in the top region above the oblate, and where the oblate has experienced the larger angular change $\Delta\Theta$ as shown in fig. 5 (top). The Reynolds number calculated from the oblate's diameter and terminal velocity is $Re = 128$. We point out that the vortex structure is obtained also in the work of Belmonte et al, [13] where a shedding vortex created by the zigzag motion of the falling strip is seen in the left figure 6.

B. Steady-Falling Oblate: Change in the Initial Height.

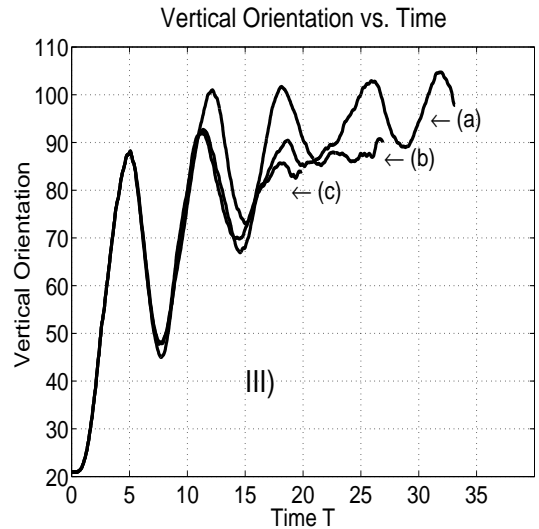
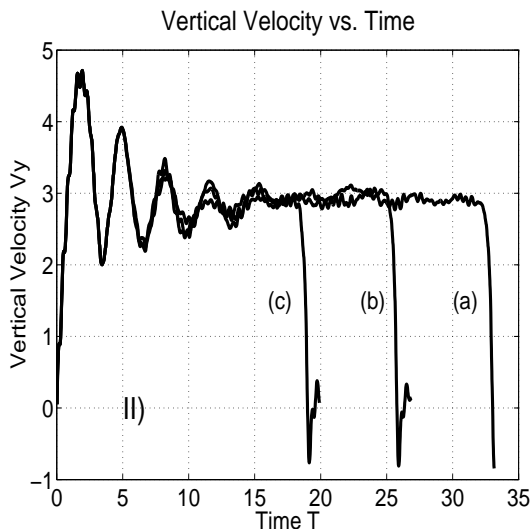
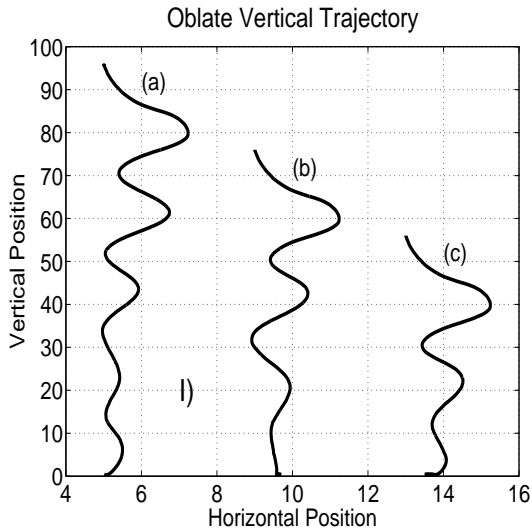


FIG. 6. Initial conditions of the system. $\theta_o = 26.6^\circ$, $\Delta r = 0.25$, $\mu = 0.033$. Each Trajectory has different initial height (a) $h_o = 96\text{cm}$, (b) $h_o = 76\text{cm}$, (c) $h_o = 56\text{cm}$. I) The spatial trajectory in the vertical plane. II) Vertical velocity vs. time. III) Vertical orientation vs. time.

We choose three different initial heights fig. 7I, (fixing the rest of parameters). If we superpose the trajectories in fig. 7I, it can be shown that there is no variation in the wavelength or in the peak-to-peak amplitude. For all the heights, the trajectories generated are in good agreement with a damped harmonic oscillation.

For the range of falling heights used, the oblate attains the same terminal vertical velocity fig. 7II, ($3\frac{\text{cm}}{\text{s}}$), its magnitude is independent on the falling height. The vertical velocity finally, reaches a stable state (uniform and linear motion), after the same time ($\sim 20\text{s}$ fig 7II). We also see that the vertical velocity suddenly becomes zero when the oblate touches the bottom.

We see in fig. 7 III(c-a), an increase in the final angle with respect to the initial height. For $h_o = 56$ the smaller height, we obtain $\sim 85^\circ$ and for larger one $h_o = 96$, we have $\sim 95^\circ$. For the larger height the oblate is still in a transitory state before it arrives to its final angle fig. 7III.

C. Steady-falling oblate: Change in the dynamical viscosity.

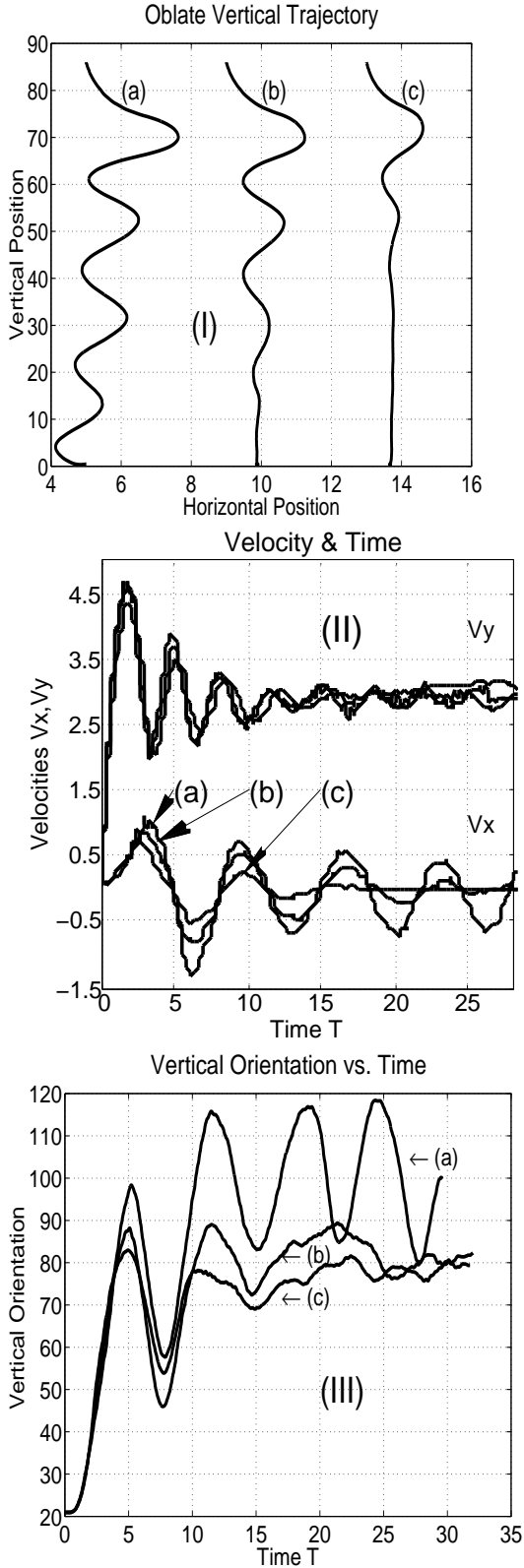


FIG. 7. Initial conditions in the system. $\theta_o = 26.6^\circ$, $h_o = 80$, $\Delta r = 0.25$. Each trajectory has a different dynamical viscosity (a) $\mu = 0.025$, (b) $\mu = 0.033$, (c) $\mu = 0.100$. I) Projection of the trajectory in the vertical plane. II) Vertical (top) and horizontal (bottom) velocities vs. time. III) Vertical orientation vs. time.

The oblate starts its swinging motion with a given initial orientation $\theta_0 = 26.6^\circ$. It glides downwards and to the side acquiring some amplitude, while the dynamical viscosity μ acts reducing the subsequent amplitudes of oscillation (fig. 8I). As we increase the dynamical viscosity from (a) $\mu = 0.025$ to (c) $\mu = 0.100$ the attenuation in the oscillatory trajectory becomes stronger. In fig. 8I a, there is a weak damping producing a long oscillatory behavior and in fig. 8I c, the trajectory is quickly attenuated in the first half of the falling height, and hereafter it follows a vertical trajectory. Similar decreasing oscillations, are observed when one small sphere suspended from a fixed point by a string or a rod, oscillates against the air and generates a damped harmonic oscillator.

The behavior of the vertical velocity is shown in fig. 8II. There is a clear damping in the peak-to-peak velocity amplitude, in all the cases. The attenuation in the vertical velocity amplitude and the time between two consecutive turning points are not very different from each other, as the fluid dynamical viscosity is changed. For the three viscosities the oblate acquires approximately the same final mean velocity $v_y = 3 \frac{cm}{s}$.

A larger variation in the velocity is observed in its horizontal component fig. 8II. There is a strong attenuation in the curve for larger viscosities fig. 8IIc. One explanation is that the interaction between the walls and the oblate is smaller when the viscosity is decreased [22]. This is also supported by the larger angular variation $\Delta\theta$ in fig. 8IIc, for smaller viscosities.

In fig. 8 III we see that the first peak-to-peak amplitudes are nearly the same for all considered viscosities. For $\mu = 0.025$ the subsequent peak-to-peak amplitudes attain a constant value of $\Theta_{p-p} \sim 15^\circ$ while for higher viscosities periodic oscillations are replaced by erratic motion of low amplitude.

D. Steady-Falling Oblate: Change in the Aspect-Ratio of the Oblate.

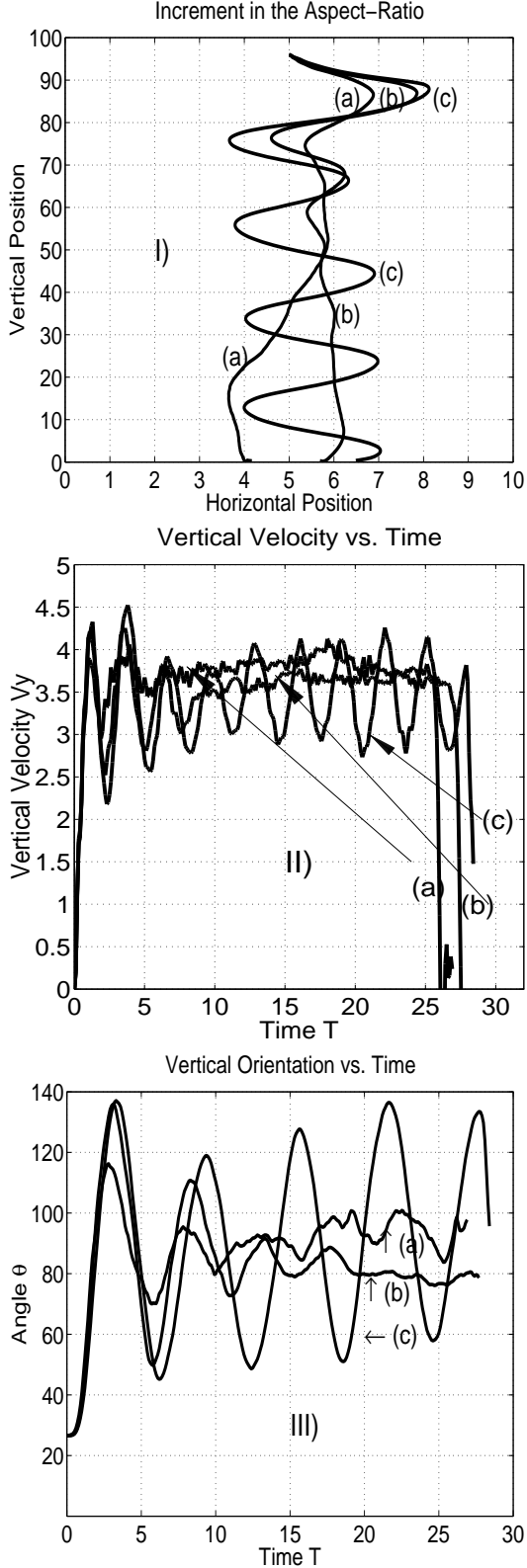


FIG. 8. Initial conditions of the system. $\Theta_o = 26.6^\circ$, $h_o = 96$, $L_x \times L_y \times L_z = 10 \times 100 \times 10$, $\mu = 0.033$. Each trajectory has different aspect-ratio (a) $\Delta r = 0, 29$, (b) $\Delta r = 0, 22$, (c) $\Delta r = 0, 18$. I) Trajectory for the vertical plane. II) Vertical velocity vs. time. III) Vertical orientation vs. time.

When the oblate's falling motion begins, the oblate gains a larger oscillation amplitude in its oscillatory falling trajectory. And for all the three trajectories presented in fig. 9, this first amplitude decreases $A_o = 3.0, 2.8, 1.8 \text{ cm}$ as the oblate's aspect-ratio is increased $\Delta r = 0.18, 0.22, 0.29$ respectively. This first large oscillation is a common characteristic for these trajectories. As the aspect-ratio is incremented, the number of cycles and the amplitude of the trajectories change. For $\Delta r = 0.22$ the trajectory presents a well defined steady-falling behavior, fig. 9I(b), but, if the aspect-ratio increases, ($\Delta r = 0, 29$), the trajectory varies, the peak-to-peak amplitude is quickly damped in the first half of the vertical trajectory, with the interesting observation that in the second half the trajectory doesn't have a steady-falling behavior fig. 9Ia. When $\Delta r = 0.18$, the smaller aspect-ratio, the trajectory has an oscillatory behavior fig. 9I(c), with a constant peak-to-peak amplitude of 3 cm .

Since the minor oblate radius is fixed in our simulations, when the aspect-ratio is increased $\Delta r = 0.18, 0.22, 0.29$, the oblate's area gets smaller, and the final vertical velocity increases $V_y = 3.5, 3.7, 3.9 \frac{\text{cm}}{\text{seg}}$, respectively, fig. 9II. The final vertical velocity decreases with the decrement in the aspect-ratio, since the smaller aspect-ratio presents more area against the fluid. As the aspect-ratio is increased the peak-to-peak amplitude in the vertical velocity diminishes. For the smaller aspect-ratio $\Delta r = 0.18$, we have the larger amplitude $1 \frac{\text{cm}}{\text{s}}$, and as the aspect-ratio is increased $\Delta r = 0.22$ and $\Delta r = 0.29$ the peak-to-peak amplitude tends to be much smaller.

The peak-to-peak amplitude for the vertical orientation Θ_{p-p} increases when the aspect-ratio decreases or the oblate's area increases. For $\Delta r = 0.29$ the peak-to-peak amplitude is $\Theta_{p-p} = 15^\circ$, (fig. 9a), and much smaller compared to $\Theta_{p-p} = 70^\circ$, (fig. 8c), for $\Delta r = 0.18$. In all cases the oblate at the end orients vertically (fig. 9 III).

E. Periodic Behavior of a Falling Oblate.

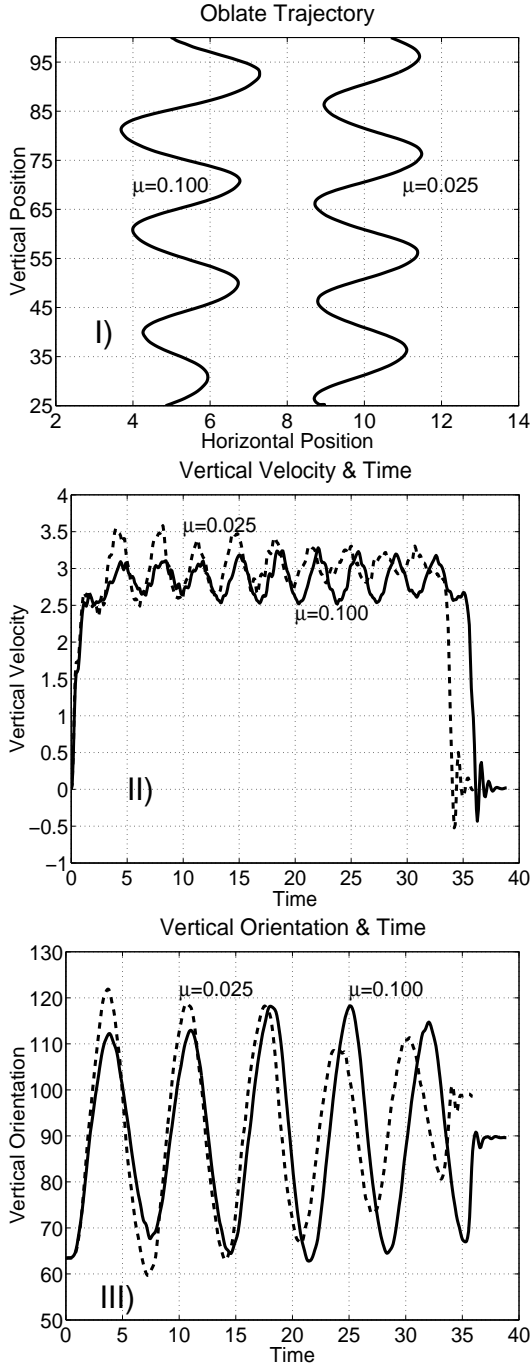


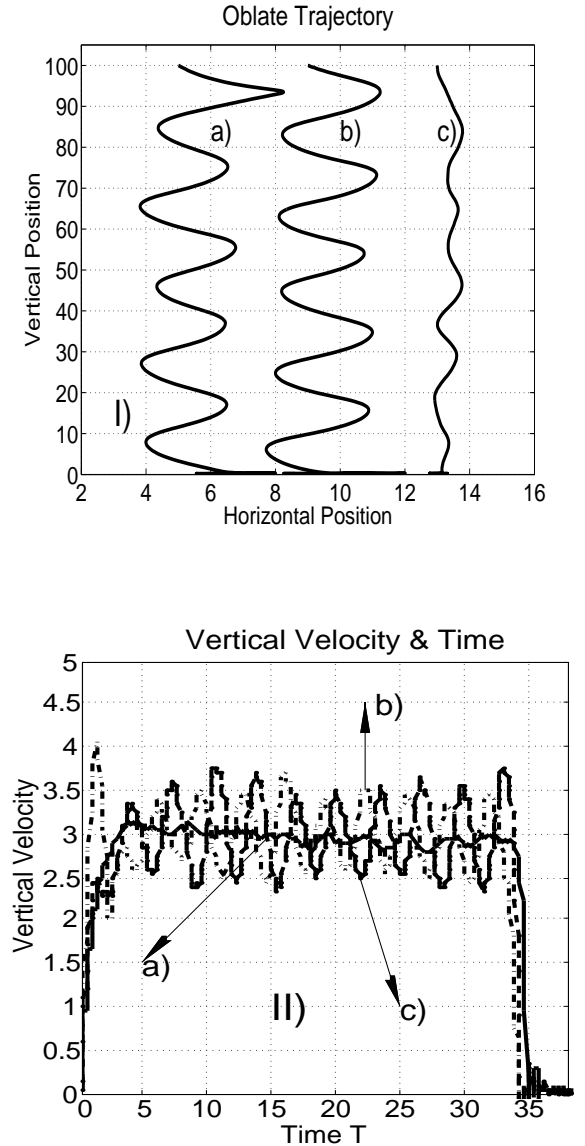
FIG. 9. Trajectories generated for $\mu_1 = 0.100$, $\mu_2 = 0.025$. (I) Trajectory in vertical and horizontal position. (II) Vertical orientation Θ vs time. (III) Vertical velocity v_y vs time. The initial conditions are $h_o = 96$, $\Delta r = 0.133$, $\theta_0 = 63.4^\circ$.

We have found periodic behavior for smaller dynamical viscosity ($Re = 480$) and smaller aspect-ratio ($\Delta r = 0.133$). The dynamics of the falling oblate is governed by inertial effects. In figure 10 (I), we show the tran-

sition from a quasi-periodic, or a long steady-falling trajectory ($\mu_1 = 0.100$), to a periodic behavior fig. 10 (I, $\mu_2 = 0.025$), when the dynamical viscosity is varied from $\mu_1 = 0.1$ to $\mu_2 = 0.025$. The trajectory presented in fig. 10I, with dynamical viscosity $\mu_2 = 0.025$ has a wave length of 20 cm.

The vertical velocity shown in fig. 10 (II), has the same transition from a long steady-falling regime with a final average velocity of $3.0 \frac{cm}{s}$ to the periodic regime where the velocity has a oscillation period of 3.3 s.

The vertical orientation presented in fig. 10 (III) has also the same transition from a long steady-falling regime to periodic behavior with a period of 6.6 s, and the angular values oscillate around $\Theta_0 = 90^\circ$ with angular peak-to-peak amplitude $\Theta_{p-p} = 60^\circ$.



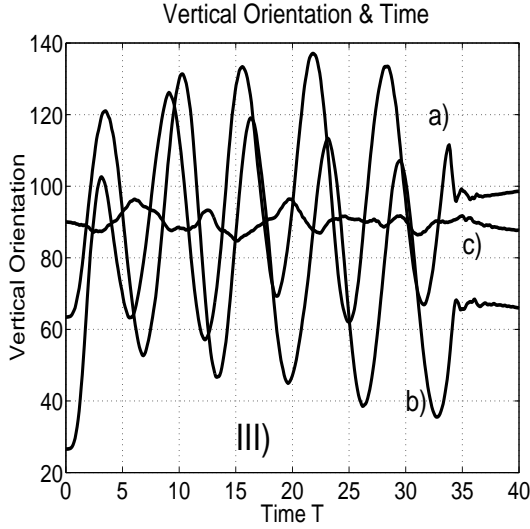
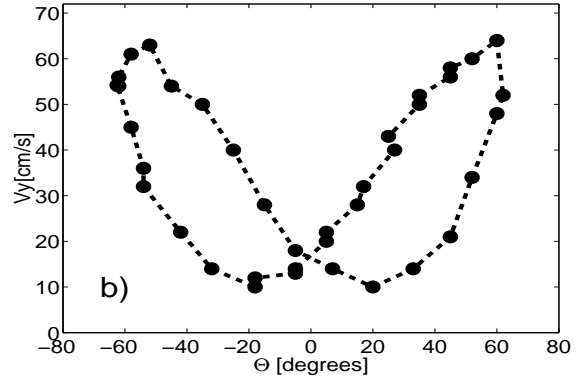
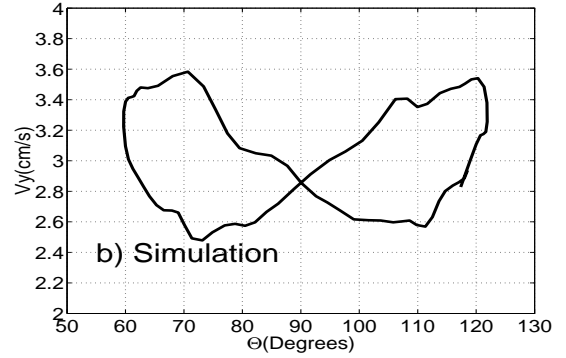
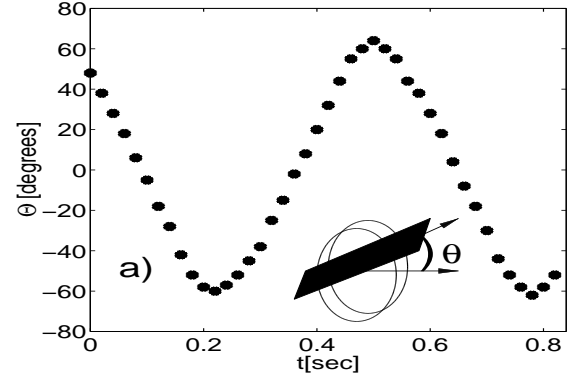
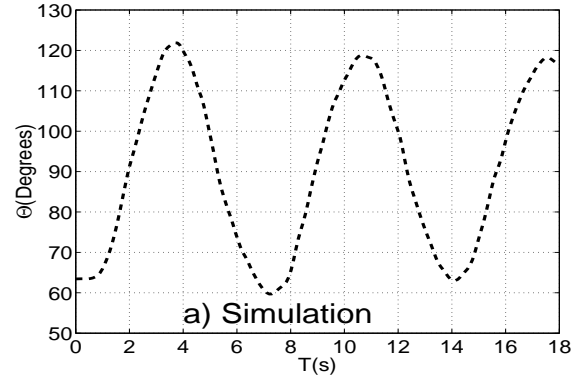


FIG. 10. I) Trajectories for three initial orientations. (a) $\Theta_0 = 26^\circ$ (b) $\Theta_0 = 63^\circ$ (c) $\Theta_0 = 90^\circ$. II) The corresponding vertical velocities. III) The vertical orientations. Initial conditions $h_o = 100$, $L_x \times L_z = 10 \times 10$, $\Delta r = 0.133$, $Re = 435$.

We perform three simulations in the periodic regime with very different initial orientation angles and the corresponding trajectories are shown in fig. 11I. In the case of $\Theta_0 = 26^\circ$ the peak-to-peak amplitude is 2.3 cm and for ($\Theta_0 = 90^\circ$) it is 0.4cm, and the oscillatory behavior is observed for the three cases. The peak-to-peak amplitude of the oscillation in the trajectory fig.10I, decreases as Θ_o is increased. In the case of the vertical velocity and orientation fig. 11III-III, the initial orientation angle also plays the same role, reducing the peak-to-peak amplitude of the curves, and for $\Theta_o = 90^\circ$ the amplitude of oscillation is the smallest of the three.

The final vertical velocity and orientation for the three trajectories are $3.0 \frac{cm}{s}$ and 85° respectively. We can say that the average final values for the vertical velocity and orientation are not modified by the variation of the initial orientation Θ_o .

We have found the largest peak-to-peak amplitude $1.0 \frac{cm}{s}$ for the vertical velocity oscillation for an initial orientation of $\Theta_0 = 26^\circ$ and it becomes smaller as the oblate's initial orientation tends to $\Theta_0 = 90^\circ$. For the peak-to-peak amplitude of the vertical orientation the oblate shows a similar behavior: we have the larger value for the amplitude $\Theta_{p-p} = 70^\circ$, and it is obtained for an initial orientation of $\Theta_0 = 26^\circ$. The smallest peak-to-peak amplitude $\Theta_{p-p} \sim 4^\circ$ is obtained for $\Theta_0 = 90^\circ$.



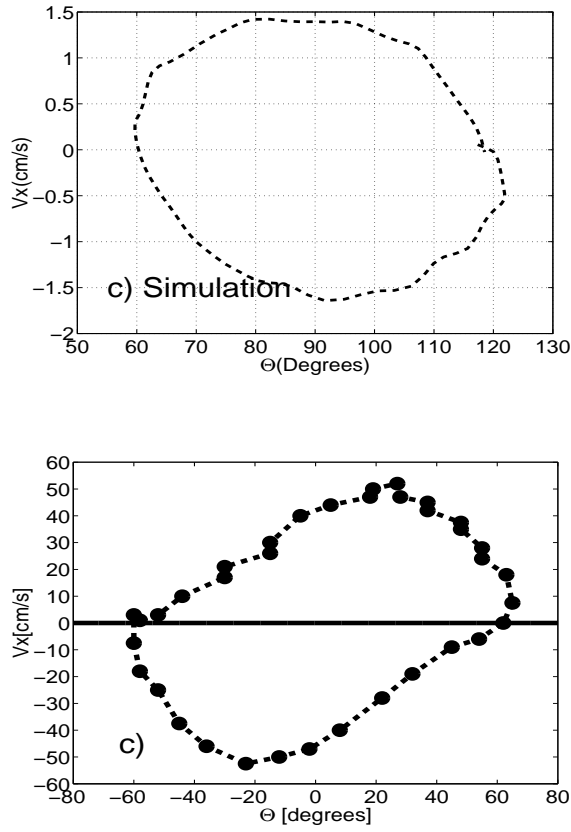


FIG. 11. Comparison with the results of Belmonte et al. ref[12] for a falling strip in the periodic regime, for the (a) Vertical orientation Θ vs time. (b) Vertical velocity V_y vs Θ . (c) Horizontal velocity V_x vs Θ . The initial conditions are $h_o = 96$, $\Delta r = 0.133$, $\mu_1 = 0.025$, $\theta_0 = 63.4^\circ$.

In figure 12a (simulation) we show the time dependence of the vertical orientation with $\mu_2 = 0.025$. The value of the angular peak-to-peak amplitude is $\Theta_o = 60^\circ$. The vertical velocity fig. 12b (simulation) reaches its maximal value $3.6 \frac{cm}{seg}$ as Θ approaches Θ_{max} , presenting a minimal drag.

The smaller vertical velocity $V_y = 2.5 \frac{cm}{s}$ in the oscillation is reached at $\Theta_{min} \sim 105^\circ$. The butterfly shape of fig. 12b was also measured in the experimental work of Belmonte et al. [13] (fig. 12b), exhibiting a vertical orientation Θ that oscillates at double the period of V_y .

The horizontal velocity oscillates around zero with the same period as Θ , presenting its maximum value at $V_{x_{max}} = 1.5 \frac{cm}{s}$ and the minimum at $V_{x_{min}} = -1.5 \frac{cm}{s}$ at $\Theta \sim 90^\circ$ as seen in fig. 12c. When the horizontal velocity is zero the oblate takes its maximum (120°) and minimum (60°) values in Θ corresponding to a non-zero value of the vertical velocity $V_y = 3.2 \frac{cm}{s}$.

F. Sensitivity to a Change in the Initial Orientation In the chaotic Regime.

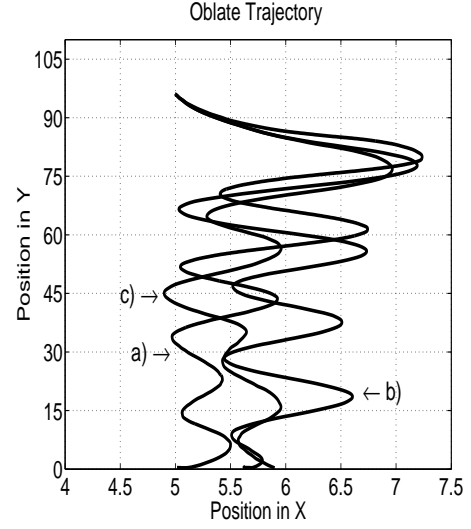


FIG. 12. Initial conditions $h_o = 96$, $\Delta r = 0.25$, $\mu = 0.033$ and tiny variations of the initial orientation (a) $\theta_0 = 26.6^\circ$, (b) $\theta_0 = 26.6001^\circ$, (c) $\theta_0 = 26.6000001^\circ$.

We can ask what is the sensitivity of the oblate to tiny changes in the initial orientation. Therefore we have simulated three trajectories shown in fig. 13, which have slightly different initial orientation. A tiny variation in the relative orientation ($\Delta\theta_o = 10^{-3}$) produces, however, a significant variation in the shape of all the curves. These can be appreciated in the lower part of the trajectories.

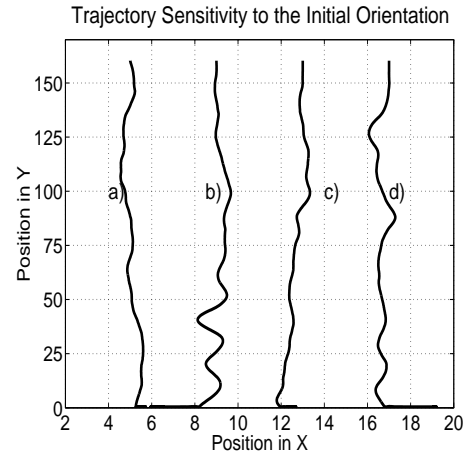


FIG. 13. Initial conditions $h_o = 166$, $\Delta r = 0.25$, $\mu = 0.033$ and tiny variations of the initial orientation (a) $\theta_0 = 45.384^\circ$, (b) $\theta_0 = 45.033^\circ$, (c) $\theta_0 = 44.981^\circ$, (d) $\theta_0 = 44.976^\circ$.

In order to get better sensitivity, we have incremented the falling height to $h_o = 166\text{cm}$. The resulting trajectories for four slightly different initial orientations in the vertical plane are presented in fig. 14. In this regime the system presents a high sensitivity to the initial orientation condition. For the four trajectories the relative angular variation is $\Delta\theta_o = 10^{-3}$.

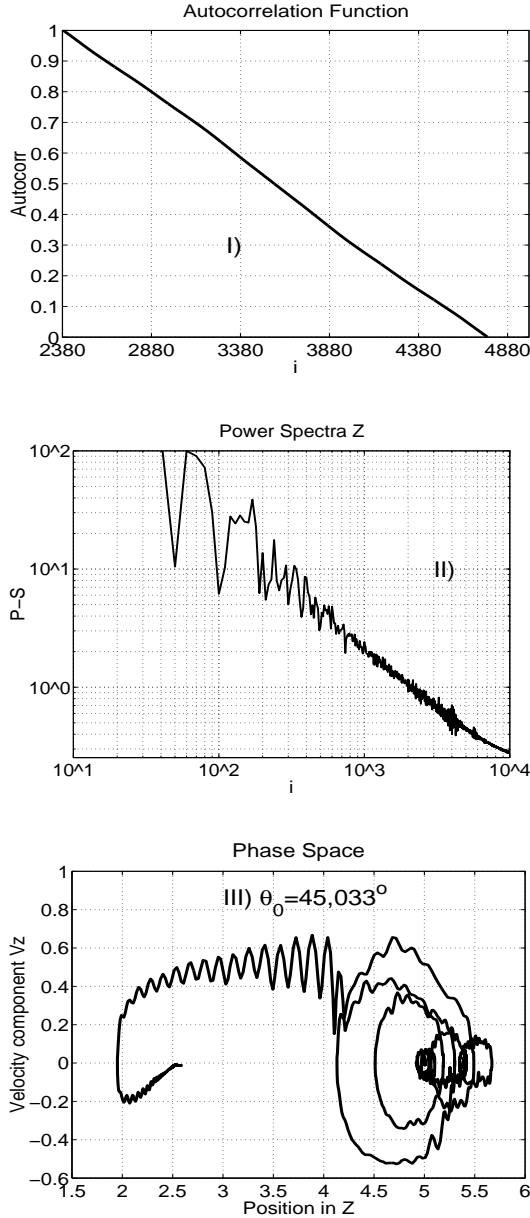


FIG. 14. Detection of chaos. I) Autocorrelation function for the time series of $x(t)$ for the trajectory of fig. 14a. II) Power Spectra of fig. 14a III) Poincaré section (p_x, x) for the trajectory of fig. 14a.

Due to this dependence on small changes in the initial orientation, we proceed to use as a tool of diagnosis, the Fourier power spectrum of the time series of the horizontal coordinate $x(t), x(t+\delta t), x(t+2*\delta t)\dots$, and in our case

$\delta t = 0.053566$. A broad spectrum of frequencies appears, as shown in fig. 15II, indicating chaotic motion.

The autocorrelation function, for the same time series (see fig. 15I), does not fall quickly to zero, it decreases linearly with time. The points are not independent of each other and a self similarity is present in the data.

In the figures 14III, we present a slices or Poincaré sections (p_x, x) , corresponding to the trajectories in fig. 14a, and which are quite irregular.

The orbits are quasi-periodic in the sense that they pass repeatedly and irregularly through the whole domain without ever closing on themselves, and without any particular time period associated with successive passages.

The sensitivity to initial conditions is clear in these four figures. A small change in the initial orientation results in large changes in position and velocity.

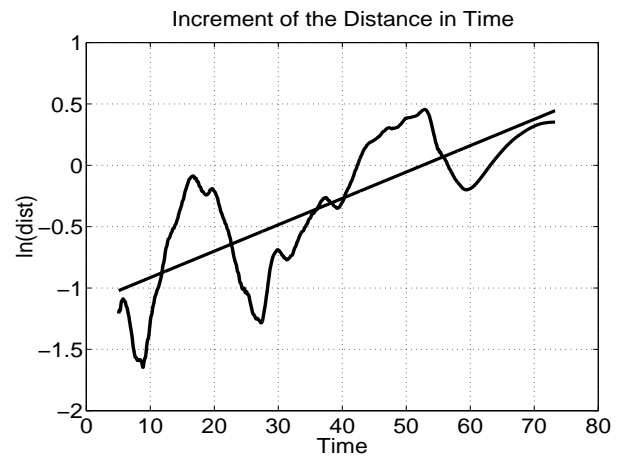


FIG. 15. Increasing logarithmic behavior for the separation distance between the trajectories (a) and (c) in fig. 14, that slightly differ in the initial orientation angle by $\Delta\Theta = 0.403^\circ$.

We can now investigate quantitatively this sensitivity by studying the increment in the Euclidean distance $d_{p_1 p_2} = \sqrt{(x_1 - x_2)^2 + (y_1 - y_2)^2}$, between the curves presented in fig. 14 (a) and (c). Fig. 16, shows that the distance between nearby points has an overall exponential time dependence $d(t) \sim \exp(\lambda t)$ and the fit gives an estimate for the Lyapunov exponent $\lambda = 0.052 \pm 0.005$. The positivity of the Lyapunov exponent is a clear indication for chaos.

G. Parameter Phase Diagram.

We explore the phase space in the dimensionless moment of inertia I^* , which is the ratio of the moment of inertia of an oblate around its principal axis to the moment of inertia of a sphere of liquid with the same diameter and the Reynolds number Re . We do a similar analysis for our results as in the work of Field, et al. [12]. It is important to remark that the mentioned experiment

was for a falling disk, with small aspect-ratio, and we expect that the dynamics of the system will be close to that of an oblate ellipsoid.

The definitions of the dimensionless variables for our system are:

$$I^* = \frac{I_{oblate}}{I_{sphere}} = \frac{5}{4} \frac{r_m \rho_{oblate}}{r_M \rho_{fluid}} = \frac{5}{4} \frac{\rho_{oblate}}{\rho_{fluid}} \Delta r \quad (13)$$

$$Re = \frac{U(2r_M)\rho_{fluid}}{\mu} \quad (14)$$

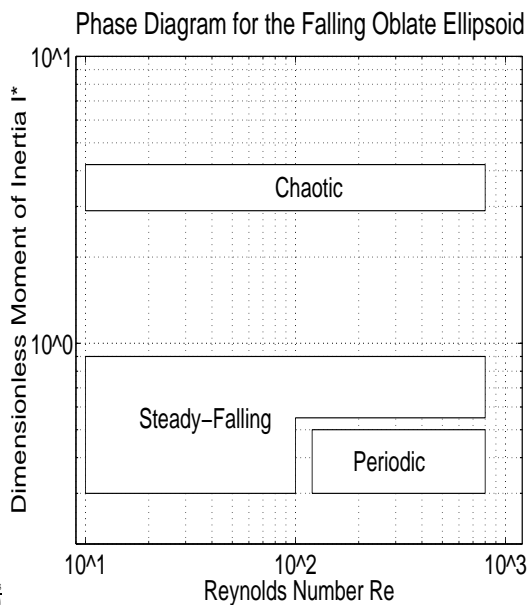
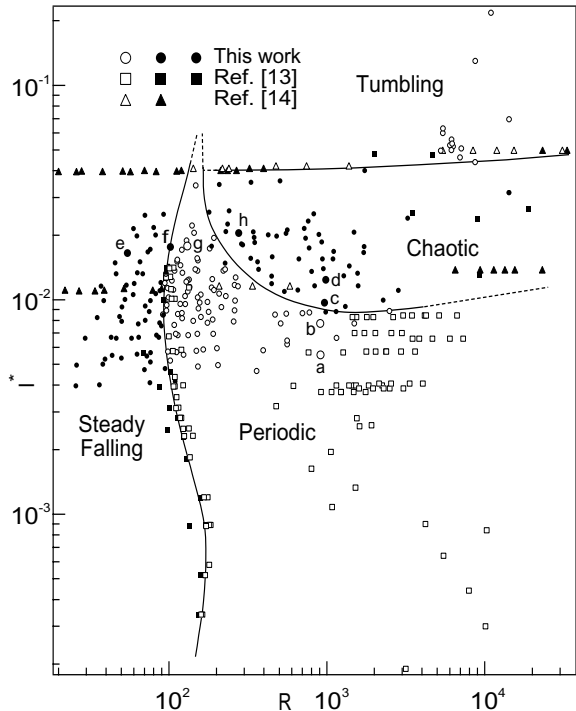


FIG. 16. The top picture shows the phase diagram of falling disks reported in ref.[11]. In the bottom plot we present the regimes of the phase space for the falling oblate obtained in our simulations.

Figure 17 bottom, shows our results. At low values of I^* and small Reynolds number (high dynamical viscosity), the left-down corner of the diagram, the motion is overdamped and the oblate drops to the bottom container without any oscillation. If the Reynolds number increases ($Re \geq 100$), fixing the moment of inertia, the trajectory is composed of successive oscillations that will decrease in amplitude until the oblate finally comes to stop at the lowest part of the container part. For all these cases this type of motion was called in our results a steady-falling, and was studied in section IIIB-B,C,D.

For small values of $I^* \sim \Delta r \ll 1$, we have a flattened ellipsoid, and Reynolds number ($Re \geq 400$), the trajectory, velocity and orientation are characterized by oscillations that repeat at equal intervals of time and space. This case was called in our simulations the oscillatory regime, and was studied in section IIIB-E.

As we increase I^* , the object will become a sphere slightly flattened in the poles, and its dynamic becomes sensitive to smaller variations in the initial orientation, exhibiting a chaotic trajectory, which is explained in section IIIF.

If we compare our diagram with the experimental results obtained by S. Field et al, ref [12] (fig. 17 top), we can see that in both pictures, the steady-falling region is located in the lower-left part, the oscillatory region is in the lower-right, and the chaotic regime is located along the top of the picture. We can say that the two diagrams are similar, but, with the difference, that the tumbling regime in the Field's diagram is not present in our results because by the comparison of the two diagrams in fig. 17. The tumbling regime would be found for larger dimensionless moment of inertia, in our case smaller aspect-ratio, demanding a larger three dimensional container and implying a very expensive computational study, than in the other regimes.

If we take a different initial orientation angle, the new phase diagram exhibits the same dynamical behavior of figure 17 bottom. The coexistence of the dynamical phases, explained above, is independent of the initial orientation of the oblate.

IV. CONCLUSIONS AND OUTLOOK

The motion of a single oblate settling in a fluid in a three dimensional container has been studied. We found three basic regimes for the dynamics of the system (steady-falling, oscillatory, and chaotic). The steady-falling and the periodic motion exhibit a similar physical behavior as observed for flattened bodies [12], [13]. With

the exception that the tumbling motion is missing in our simulations.

We have characterized the dynamics of the steady-falling regime when the dynamical viscosity, dropping height, and oblate's aspect-ratio are changed. Several conclusions can be drawn from this part of the work.

(a) The spatial trajectories (x, y) are composed of oscillations that correspond to a damped harmonic motion. This regime is present for small values of $I^* \approx 0.5 - 1$, $Re \approx 100$ and is shown in fig.6-7. There is no variation in the trajectories when we increase the initial height. When the aspect-ratio is varied, the trajectories change very much, fig. 8. The aspect-ratio dominates strongly the type of trajectory that is present in the system.

(b) The final vertical velocity V_y does not depend on the initial falling height and the dynamical viscosity.

(c) The vertical orientation Θ of the oblate, undergoes a rotational motion till its mayor axis is aligned with the direction of gravity. This tendency of finding the minimal resistance against the fluid, is present for all Reynolds numbers in the range $Re \approx 30 - 100$ used in our simulations.

The periodic behavior in our simulations is found for ($Re \sim 500$), and small ($I^* \leq 0.5$). The most important characteristic on this regime is that the vertical orientation Θ , oscillates at the double of the period of the vertical velocity V_y , and at the same period of the horizontal velocity V_x . This periodic motion is also present in the work of Belmonte et al. [13]. In this regime the initial orientation determines the value of the oscillation amplitude in the spatial trajectory (x, y) , velocity V_y and orientation Θ . For $\Theta_o = 90^\circ$ the amplitudes of the above quantities approach a smaller value.

The chaotic behavior is present for $I^* \geq 1$ and in the entire range of Reynolds numbers used in the simulation. The separation between the spatial trajectories of the falling oblate will diverge for small variations in the initial orientation Θ_o , and grows exponentially in time. The value found for the Lyapunov exponent is around $\lambda = 0.052 \pm 0.005$.

The construction of the phase diagram shows three well-defined dynamical regions as in the case of ref. [12]. But with the difference that the chaotic behavior in the above reference is associated with a transition to chaos through intermittency for which we have no indication in our simulations. The phase diagram is independent on the initial orientation.

More work to better understand the role of the fluid pressure and velocity fields as well as a more systematic study of the phase transition in the phase diagram seem necessary

V. ACKNOWLEDGMENT

This research is part of the SFB-404-Project A7. Helpful discussions with S. Schwarzer, R. Mück, and E. Kuusela are acknowledged and appreciated.

-
- [1] M. Kajikawa *J. Meteorol. Soc. Jpn.* **60** 797-803 (1982).
 - [2] R. von Mises, Theory of Flight *McGraw-Hill, New York, 1945*.
 - [3] H. J. Lugt, *Annu. Rev. Fluid Mech.* **15** 123 (1983).
 - [4] E.K. Marchildon, A. Clamenand, W. H. Gauwin *Can. J. Chem. Eng.* August, 178-182 (1964).
 - [5] M. P. Allen and D. J. Tisdlesley. Computer Simulations of Liquids. *Clarendon Press, Oxford, 1987*.
 - [6] H. Viets and D. A. Lee *A.I.A.A. Journal.* **9** ,2038-2042 (1971).
 - [7] J.C. Maxwell, *Cambridge and Dublin Math. J.* **9** ,115-118 (1853).
 - [8] H. Aref and S. W. Jones, *Phys. Fluids A.* **5** ,3026-3028 (1993).
 - [9] Y. Tanabe and K. Kaneko, *Phys. Rev. Lett.* **73** 1372-1375 (1994); **75**, 1421 (1995);
 - [10] L. Mahadevan , H. Aref, and S. W. Jones, *ibid* **75**, 1420 (1995).
 - [11] M. Bauer, S. Habip, D.R. He, W. Martiensen, *Phys. Rev. Lett.* **68** 1625-1628 (1992).
 - [12] S. Field, M. Klaus, M. Moore, and F. Nori *Nature (London)* **388**,252 (1997).
 - [13] A. Belmonte, H. Eisenberg and E. Moses, *Phys. Rev. Lett.* **81**, 345-348 (1998).
 - [14] P. Y. Huang, H. H. Hu, and D. D. Joseph, *J. Fluid Mech.* **362**, 297-325 (1998).
 - [15] M. Allen and D. J. Tildesley, Computer Simulations of liquids, (Clarendon Press, Oxford, 1987).
 - [16] W. h. Press, B. P. Flannery, S. A. Teukolsky, and W. T. Vetterling. Numerical Recipes in C. (Cambridge University Press, Cambridge, 1992).
 - [17] E. Kuusela, K. Höefler, and S. Schwarzer *J. of Engineering Mathematics* **41**,221 (2001).
 - [18] B. Wachmann, S. Schwarzer, and K. Höefler *Int. J. Mod. Phys. C* **9**, No **8**,1361 (1998).
 - [19] K. Höefler *.Simulation and Modeling of Mono- and Bidisperse Suspensions. Doctoral Thesis.Stuttgart University.* (2000).
 - [20] K. Höefler and S. Schwarzer, *Phys. Rev. E* **61**,7146 (2000).
 - [21] Aaron L. Fogelson and Charles S. Peskin, *Journal of Computational Physics* **79** 50-69 (1988).
 - [22] H. Brenner, *Chem. Eng. Sci.* **16**, 1753-1777 (1961).
 - [23] L. Mahadevan, W. S. Ryu, A. D. T. Samuel, *Phys. Fluids* **11**, 1-3 (1999).